

Spatial-Temporal Enhanced Transformer Towards Multi-Frame 3D Object Detection

Yifan Zhang, Zhiyu Zhu, Junhui Hou

Abstract—The Detection Transformer (DETR) has revolutionized the design of CNN-based object detection systems, showcasing impressive performance. However, its potential in the domain of multi-frame 3D object detection remains largely unexplored. In this paper, we present STEM, a novel end-to-end framework for multi-frame 3D object detection based on the DETR-like paradigm. STEM treats multi-frame 3D object detection as a sequence-to-sequence task and effectively captures spatial-temporal dependencies at both the feature and query levels. Specifically, to model the inter-object spatial interaction and complex temporal dependencies, we introduce the spatial-temporal graph attention network, which represents queries as nodes in a graph and enables effective modeling of object interactions within a social context. To solve the problem of missing hard cases in the proposed output of the encoder in the current frame, we incorporate the output of the previous frame to initialize the query input of the decoder. Moreover, to mitigate the issue of redundant detection results, where the model generates numerous overlapping boxes from similar queries, we consider an IoU regularization term in the loss function, which can distinguish between queries matched with the ground-truth box and queries that are similar but unmatched during the refinement process, leading to reduced redundancy and more accurate detections. Through extensive experiments, we demonstrate the effectiveness of our approach in handling challenging scenarios, while incurring only a minor additional computational overhead. Our framework will potentially bring insights to this field. The code will be available at <https://github.com/Eaphan/STEM>.

Index Terms—Multi-Frame 3D Object Detection, Transformer, Graph Attention Network, Point Cloud, Autonomous Driving.

1 INTRODUCTION

THREE-dimensional (3D) object detection is one of the fundamental tasks in the computer vision community that aims to identify and localize the oriented 3D bounding boxes of objects in specific classes. It plays a critical role in broad applications, including autonomous driving, object manipulation, and augmented reality. Recent years have witnessed the emergence of a large number of deep learning-based single-frame 3D detectors [1], [2], [3] with the advent of large-scale datasets [4], [5]. Nonetheless, given the intricacies of traffic environments, including long distances and inter-object occlusion, the object information encapsulated within point clouds may be inevitably subject to distortions of potential sparsity or incompleteness. Consequently, these aspects typically engender a sub-optimal performance of the single-frame 3D detectors [6].

As the point cloud sequence intrinsically provides multiple views of objects, it implies promising approaches to extract vital spatiotemporal information for facilitating more accurate detection, especially for objects that pose significant detection challenges. By incorporating complementary information from other frames, a multi-frame 3D object detector exhibits improved performance compared to a single-frame 3D object detector (see Fig. 1).

The existing works in multi-frame 3D object detection have explored some feasible solutions. A straightforward one is concatenating the observed points from multiple frames and using an additional dimension to indicate the timestamp [5]. However, this method lacks explicit mod-

eling of cross-frame relations and is less effective for fast-moving objects given multi-frame point cloud input [7]. Some previous works naturally apply the long short-term memory (LSTM) network or gated recurrent unit (GRU) to voxel-level or BEV-level features for temporal modeling [8], [9]. 3D-MAN [7] stores the features of box proposals in a memory bank and performs attention across proposal features from multiple perspectives. Recently some high-performance methods [10], [11] adopt a two-phase framework for multi-frame 3D object detection, where a baseline detector is employed to generate boxes and speed of objects in each frame, and the detected boxes across frames are associated to form a trajectory; Then a specific region-based network is proposed to refine the box based on sequence object points and boxes. Despite the gratifying success of these approaches, such two-phase pipelines for multi-frame object detection are somewhat sophisticated, requiring many extra hand-crafted components, e.g., IoU-based proposal matching, per-frame feature encoding, and trajectory-level feature propagation [10]. Thus, there is a pressing need to construct a novel framework for multi-frame 3D object detection that not only yields accurate results but also operates in a fully end-to-end fashion.

The recent advancements in sequential modeling [12] and cross-modal fusion [13], [14] reveal the remarkable capabilities of the Transformer architecture as a powerful framework for effectively modeling the information interaction within sequential or cross-modal data. The intrinsic self-attention module in Transformer plays a critical role in this success, as it enables the effective encoding of mutual relationships within the data. Especially, DETR [15] employs a transformer-based architecture to directly predict the bounding boxes and categories of objects,

- Y. Zhang, Z. Zhu, and J. Hou are with the Department of Computer Science, City University of Hong Kong, Hong Kong. E-mail: yzhang3362-c@my.cityu.edu.cn; zhiyuzhu2-c@my.cityu.edu.hk; jh.hou@cityu.edu.hk;

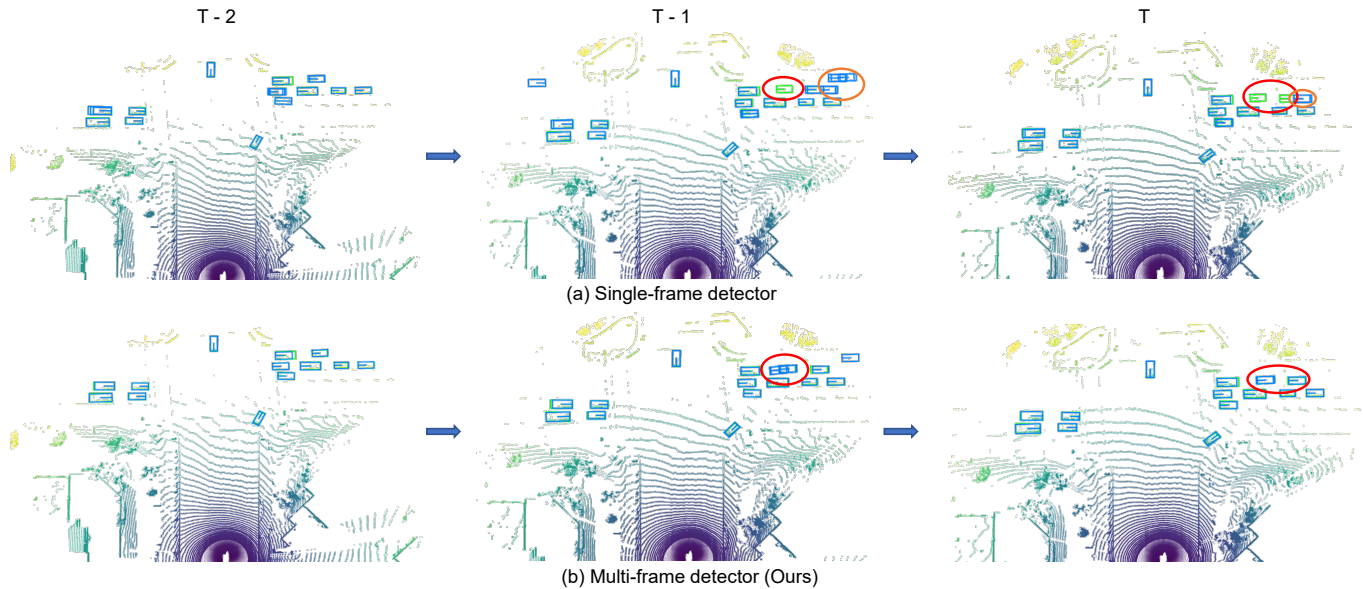


Fig. 1: The figure illustrates a comparison between our method and a single-frame detector [6] in a challenging outdoor 3D object detection scenario. Ground truth boxes are highlighted in green, while predicted bounding boxes are shown in blue. As highlighted within red circles, Our method leverages additional temporal information to successfully detect several heavily occluded objects, which the single-frame detector fails to detect. Moreover, there are more false-positive predictions in the result of the single-frame detector, as highlighted in orange circles. Best viewed in color.

which replaces traditional convolutional neural network (CNN)-based detectors [16], [17] and achieves state-of-the-art performance [18]. The Transformer architecture is well-suited for multi-frame 3D object detection. *First*, consecutive frames contain valuable temporal information about the motion and behavior of objects. Transformer excels at modeling sequential data by capturing long-range dependencies in both spatial and temporal dimensions, which is crucial for understanding object dynamics across multiple frames [19], [20]. *Second*, DETR-like detectors operate in a fully end-to-end manner, enabling direct optimization of the entire multi-frame 3D object detection pipeline. This end-to-end learning manner avoids separate modules or handcrafted components, such as extra feature encoding networks or post-processing steps. Given the above factors, we propose **STEMD**, a novel end-to-end multi-frame 3D object detection framework based on the DETR-like paradigm in this paper. And we enhance the model from *three* aspects specifically tailored for multi-frame 3D object detection, i.e., *graph-based spatial-temporal modeling*, *improved query initialization*, and an effective *regularization term*, as detailed subsequently.

1) It has been widely acknowledged that scene understanding tasks, such as pedestrian trajectory prediction [19], [20], [21], heavily rely on the effective modeling of spatial-temporal relationships between individual objects and their surroundings. For example, in crowded environments, pedestrians exhibit diverse interaction patterns, such as avoiding collisions, following groups, or adapting to dynamic obstacles. However, in the context of multi-frame 3D object detection, we argue that the self-attention mechanism employed in the decoder of DETR fails to fully exploit the relations among queries. This limitation arises due to the dense application of self-attention across all queries. **To address this issue**, we propose a graph-based attention

network that leverages the complex spatial dependencies among objects. In our approach, we represent single objects (queries) as nodes and model their interactions as edges in a graph structure (as shown in Fig. 2). By allowing nodes to dynamically attend to neighboring nodes in a context-aware manner, our graph-based attention network captures intricate interactions. This attention mechanism facilitates the learning of various social behaviors, enabling our model to adapt to complex scenarios and make accurate predictions. Moreover, we introduce the graph-to-graph attention network to effectively model temporal dependencies. This enables our model to make current temporal predictions that satisfy the sequential consistency of object trajectories by attending to relevant past position information.

2) In existing DETR-like models [22], the encoder generates a set of region proposals, and the decoder progressively refines the bounding box predictions based on those queries initialized with these proposals. However, it is challenging to obtain accurate results for these cases through layer-by-layer refinement in the decoder if the initial queries inferred from the encoder miss some corner cases. Since these cases may be more easily detectable in preceding frames, we propose to initialize additional input queries for the decoder in the present frame using selected final predicted boxes from the preceding frame. Consequently, this initialization yields a higher recall rate of queries with respect to ground truth boxes and provides a strong starting point for refining the bounding box predictions. This strategy, namely Temporal Query Recollection (TQR), helps in handling object occlusions, sudden disappearance, and other challenging scenarios commonly encountered in point cloud sequences. Besides, initializing the queries with the final predicted boxes from the previous frame promotes temporal consistency in graph-based learning.

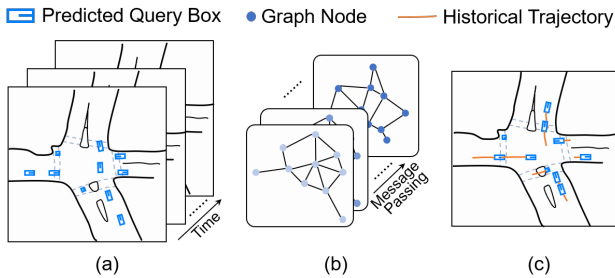


Fig. 2: (a) Visualization of the multi-frame point clouds and the corresponding predicted query boxes within a scene. (b) Our approach represents the queries as nodes in a graph and utilizes the graph attention network (GAT) to effectively capture spatial-temporal dependencies. (c) The incorporated attention mechanism enables the model to learn interaction patterns among objects, empowering it to comprehend diverse social behaviors like collision avoidance, group following, adaptation to dynamic obstacles, and make precise predictions at current frame even in complex scenarios.

3) Existing DETR-based detectors [15], [22] utilize the one-to-one Hungarian Matching method, which assigns each ground truth box to the query with the highest IoU and treats other highly similar queries as negative samples. But the current loss supervision for individual queries lacks consideration for surrounding queries, which poses difficulties in distinguishing between the best match and other highly similar queries. Similar queries are insufficiently suppressed and turn into redundant prediction boxes. Furthermore, the presence of duplicate query boxes without Non-Maximum Suppression (NMS) can negatively impact detection accuracy. To tackle these issues, we introduce an IoU regularization term that penalizes query boxes in close proximity to one another. This regularization encourages unmatched queries to differentiate their predicted bounding boxes from the best match, resulting in distinct refinements and less redundant prediction boxes.

We conduct extensive experiments on the prevailing Waymo dataset [4]. Our novel approach surpasses the performance of previous state-of-the-art single-frame and multi-frame 3D object detectors by a significant margin, while incurring only a tiny additional computation cost.

To summarize, the principal contributions of this research can be encapsulated as follows:

- we present a novel DETR-like framework for multi-frame 3D object detection, namely STEMMD, which captures the spatial-temporal dependencies in the sequence at both feature and query levels;
- we propose to effectively model the socially-aware inter-object spatial interaction and complex temporal dependencies with a spatial-temporal graph attention network (STGA-Net), which represents queries as nodes in a graph;
- we propose TQR, a simple yet effective training strategy that enhances the initial query input of the decoder in the current frame using final predicted boxes from the previous frame; and
- we introduce an IoU regularization term to penalize

query boxes with large overlaps, encouraging similar queries to output fewer redundant boxes as the ground-truth boxes in BEV generally do not overlap.

The remainder of the paper is organized as follows. Sec. 2 reviews existing works most related to this work. In Sec. 3, we introduce the overall architecture of STEMMD and elaborate on its key components. In Sec. 4, we validate the effectiveness of our proposed method on the Waymo dataset and conduct ablation studies to analyze the effect of different components. Finally, Sec. 5 concludes this paper.

2 RELATED WORK

In this section, we mainly review existing works on single-frame 3D object detection, multi-frame 3D object detection, graph structure learning, and vision transformer, which are closely aligned with the core objectives of our work.

Single-frame 3D Object Detection. Early research on single-frame 3D object detection can be classified into voxel-based and point-based approaches. Typically, voxel-based 3D detectors turn point clouds into grid-structure forms with fixed sizes and employ sparse convolution networks for feature extraction [1], [23], [24]. PointPillar [2] deployed a novel encoder that learns features on pillars (vertical columns) of the point clouds, where only 2D convolutional layers are used in the network. Point-based 3D detectors [16], [25] consume the raw 3D point clouds directly and extract highly semantic features through a series of downsampling and set abstraction layers following PointNet++ [26]. To preserve foreground points as much as possible, [27] and [28] optimized the downsampling strategies with semantic information. There are also approaches that leverage a hybrid representation by integrating the multi-scale voxel-based features and point-based features containing accurate location information, and thus achieve a balance between detection accuracy and efficiency [3], [29]. PDV [30] efficiently localizes voxel features with voxel point centroids, which are then aggregated through a density-aware RoI grid pooling module using kernel density estimation and self-attention with point density positional encoding. Besides, some works convert point clouds into range view representations and process them with more efficient 2D CNN [31], [32].

Multi-frame 3D Object Detection. It has been proven in existing state-of-the-art works, given short point cloud sequence input, the simple concatenation of multi-frame point clouds can significantly outperform the single-frame detection [6], [33]. However, this strategy lacks explicit modeling of cross-frame relations and is less effective for fast-moving objects given a long point cloud sequence [7], [10]. Naturally, some early works applied LSTM or GRU to voxel-level or BEV-level feature maps across different frames for temporal modeling [8], [9]. Recently some high-performance methods [10], [11] adopt a two-phase framework for multi-frame 3D object detection, where a baseline detector is employed to generate boxes and speed of objects in each frame, and the detected boxes across frames are associated to form a trajectory; Then a specific region-based network is proposed to refine the box based

on sequence object points and boxes. Despite the gratifying success of these approaches, such two-phase pipelines for multi-frame object detection are somewhat sophisticated, requiring many extra hand-crafted components, e.g., IoU-based proposal matching, per-frame feature encoding, and trajectory-level feature propagation [10].

Graph Structure Learning. Graph neural networks (GNNs) have emerged as powerful tools for learning intrinsic representations of nodes and edges in graph-structured data [34]. GNNs excel at capturing rich relationships among nodes and enabling comprehensive analysis of graph data. Graph convolution networks (GCNs) have revolutionized graph analysis by extending the conventional convolution operator from regular domains to handle arbitrary and unordered graph-structured data [35]. GCNs encompass spatial-based methods [36], [37] and spectral-based approaches [38], employing a recursive message-passing scheme to project graph data into a continuous and low-dimensional space [36]. Building on this success, Velickovic *et al.* [39] introduced graph attention networks, which incorporate attention mechanisms to selectively attend to neighboring nodes during message passing. GATs have demonstrated improved performance in tasks such as node classification, link prediction, and graph classification [40]. GNNs have also been proven effective in various computer vision tasks. For example, Xu *et al.* [41] proposed SGRN, which learns a spatial-aware sparse graph to leverage semantic and spatial layout relationships in object detection. Yu *et al.* [20] presented a spatiotemporal graph transformer framework for modeling social interactions and complex temporal dependencies in pedestrian trajectory prediction. Additionally, GCNs have achieved remarkable performance in action recognition by modeling human body skeletons as spatiotemporal graphs [42], [43]. Inspired by these works, we propose to use a spatial-temporal graph attention network to mine the relationships between queries in the decoder at the current frame and previous frames. We leverage learned local interactions and temporal information to comprehensively understand the scene and make precise predictions, even in challenging scenarios.

Vision Transformer. Transformer-based models have gained significant popularity in recent years across various deep learning tasks. Initially utilized in Natural Language Processing (NLP) [12], [44], [45], these models have witnessed success in computer vision tasks as well [15], [46], [47]. The intrinsic self-attention module in Transformer plays a critical role in this success, as it enables the effective encoding of mutual relationships within the data. Especially, DETR presented a novel paradigm shift by formulating object detection as a direct set prediction problem [15]. The core idea behind DETR lies in its ability to leverage the self-attention mechanism for capturing global context and modeling the relationships between objects in an image. Subsequently, Deformable DETR [22] enhanced DETR by incorporating a deformable attention module that focuses on a small set of salient key elements in the feature map. Recently, some methods have also applied the transformer to 3D object detection tasks [8], [48], [49], [50], [51]. The ability of transformers to capture long-range dependencies

and rich temporal information has made them a natural fit for multi-frame 3D object detection. By considering the motion and behavior of objects across frames, transformers can provide valuable insights into the dynamics of 3D objects.

3 PROPOSED METHOD

3.1 Overview

As illustrated in Figure 3, architecturally, our framework follows the DETR-like paradigm and comprises several integral components, including a CNN-based backbone, an encoder, a decoder, and multiple FFN (Feed-Forward Network) prediction heads. Furthermore, our framework incorporates convolutional GRU (ConvGRU) and spatial-temporal graph attention network, which are adopted to model feature-level and query-level spatial-temporal dependencies, respectively. Specifically, our proposed model takes a long-term point cloud sequence of T frames as input, denoted as $\{I_1, \dots, I_T\}$. To eliminate the influence of ego-motion, we leverage the LiDAR pose information to align the point cloud of previous frames. Then, point cloud I_t in each time step t is voxelized and forwarded to a sparse 3D convolution network to obtain the BEV features X_t . And we further perform local self-attention with BoxAttention [52] in the encoder module, followed by a ConvGRU block to model spatial-temporal dependencies and obtain enhanced encoder features H_t . After that, a class-agnostic FFN is applied to generate object proposals based on the enhanced encoder features H_t , and the top N_p scored proposals are selected to initialize the queries for the decoder. In the decoder layers, we perform self-attention between queries and cross-attention between queries and the enhanced encoder features H_t [22]. Here, the output of each decoder layer is then passed through a detection head to conduct iterative box refinement. Particularly, we propose a spatial-temporal graph attention network to capture both the spatial relationship between queries in each frame and temporal dependencies between queries of adjacent frames. The enhanced graph embeddings are further passed to another detection head to obtain final predictions. Besides, to reduce the impact of the encoder missing hard cases in its proposal predictions, we select top N_{res} scored prediction boxes of last frame to supplement these proposals as extra query input of decoder in current frame (see details in Sec. 3.4).

In what follows, we will introduce the key components in detail.

3.2 ConvGRU-based Feature Enhancement for Encoder

The BEV features extracted by the CNN backbone, along with corresponding positional embeddings, are sent to the encoder. This allows for the capture of local structures and contextual information in the BEV representation using a local self-attention mechanism, resulting in the generation of X_t^E . In addition to the standard encoder, we incorporate ConvGRU to capture both spatial and temporal information from sequential 2D BEV feature maps $\{X_t^E\}_{t=1}^T$, resulting in enhanced encoder features denoted as H_t . The ConvGRU

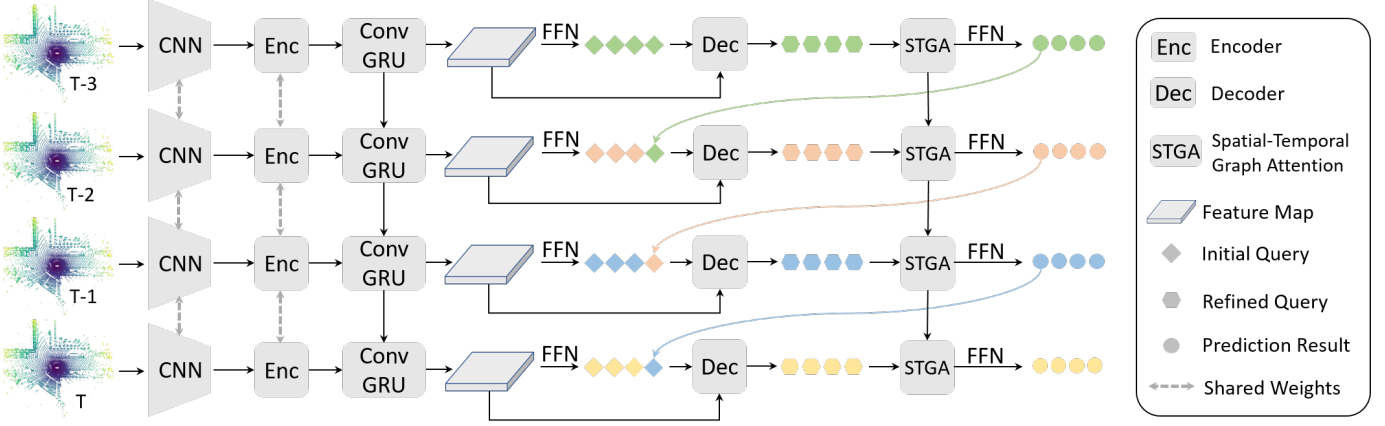


Fig. 3: The framework of the proposed STEMD. The multi-frame point clouds are fed into the network as a sequence, and a shared CNN extracts features of each frame. Then the encoder performs local self-attention to enhance the features, followed by a ConGRU block to model the feature-level temporal dependencies (see § 3.2). Next, a class-agnostic FFN is applied to generate object proposals, which are utilized to initialize the query input of the decoder. Subsequently, we use a graph attention network to capture both spatial and temporal dependencies among queries across different frames (see § 3.3). Especially, we select the high-scored final prediction of last frame as extra query input of the decoder in current frame, to mitigate the effect of the encoder missing hard cases in its predicted proposals (see § 3.4). The STEMD could be trained in a fully end-to-end manner.

model consists of two main components: the convolutional component and the GRU component [53]. The convolutional component is able to extract spatial features from each input feature map, while the GRU component is responsible for modeling the temporal dependencies between the feature maps at different time steps. The output H_t of ConvGRU at each time step t is obtained by:

$$\begin{aligned} R_t &= \sigma(\text{Conv}(H_{t-1}, U_r) + \text{Conv}(X_t, W_r) + b_r), \\ Z_t &= \sigma(\text{Conv}(H_{t-1}, U_z) + \text{Conv}(X_t, W_z) + b_z), \\ \tilde{H}_t &= \tanh(\text{Conv}(R_t \odot H_{t-1}, U_h) + \text{Conv}(X_t, W_h) + b_h), \\ H_t &= Z_t \odot H_{t-1} + (1 - Z_t) \odot \tilde{H}_t, \end{aligned} \quad (1)$$

where $\text{Conv}(\cdot, \cdot)$ denotes the convolution operation, X_t is the input feature map at time t , $\sigma(\cdot)$ represents the sigmoid activation function, \odot denotes element-wise multiplication, R_t and Z_t are the reset gate and update gate vectors, respectively, \tilde{H}_t is the candidate hidden state at time t . In these equations, H_{t-1} is the hidden state at time $t-1$, U_r , W_r , U_z , W_z , U_h , W_h represent the GRU weights, and b_r , b_z , b_h are the biases.

The enhanced feature H_t is then utilized to generate initial object proposals B_t^E through a feed-forward network (FFN) head. With the N_q object queries Q_t initialized with boxes including selected top N_p scored box proposals, we perform self-attention between queries Q_t and cross-attention between query Q_t and the enhanced encoder features H_t to update the queries layer-by-layer [22]. We implement the encoder and decoder following existing work [18], [22], [54], and describe them in this section making this paper self-contained.

3.3 Spatial-Temporal Graph Attention Network

Modeling spatial-temporal relationships between individual objects and their surroundings helps to understand complex

scenarios and social interaction, thus yielding accurate detection results in current frame. As illustrated in Fig 4, we first introduce how to eliminate redundant bounding boxes output from the upstream decoder and derive representative queries for constructing graphs. Next, we use the graph attention network to capture both *spatial* relation between queries in a single frame and the *temporal* dependencies between queries of adjacent frames.

3.3.1 Graph Node Selection

Redundant or overlapping bounding boxes predicted by the decoder can hinder the learning of graph structure topology and deteriorate the overall performance. To solve this problem, we propose an efficient method in this section, outlined in Algorithm 1, to eliminate redundant bounding boxes and retain the filtered results as nodes in downstream graph attention modules. By doing so, we ensure that the selected bounding boxes effectively cover distinctive and representative regions of interest in the input data. This approach enhances the performance of graph-based learning and facilitates a more comprehensive understanding of the underlying relationships and structures within the scene.

Let $\mathcal{B}_t^D = \{b_{t,i}^D\}_{i=1}^{N_q}$, $\mathcal{S}_t^D = \{s_{t,i}^D\}_{i=1}^{N_q}$, and $\mathcal{Q}_t^D = \{q_{t,i}^D\}_{i=1}^{N_q}$ denote the predicted boxes, confidence scores, and query embeddings of the decoder at time t , respectively. First, given a bounding box $b_{t,i}^D$, we define his neighboring sets $\mathcal{N}_{b_{t,i}^D}$, where $\text{IoU}(b_{t,i}^D, b_{t,j}^D) > \theta$ for each $j \in \mathcal{N}_{b_{t,i}^D}$. These neighboring sets contain boxes that overlap significantly with the given box. Second, we select the neighboring box $b_{t,m}^D$ with the highest confidence score, denoted as $b_{t,m}^D$ where m is the index of the neighboring box with the highest confidence score. Next, if the neighbors are not empty we update the confidence of $b_{t,i}^D$ as follows:

$$\tilde{s}_{t,i}^D = \begin{cases} s_{t,i}^D, & \text{if } s_{t,i}^D \geq s_{t,m}^D \\ s_{t,i}^D \times (1 - \text{IoU}(b_{t,i}^D, b_{t,m}^D)), & \text{if } s_{t,i}^D < s_{t,m}^D \end{cases} \quad (2)$$

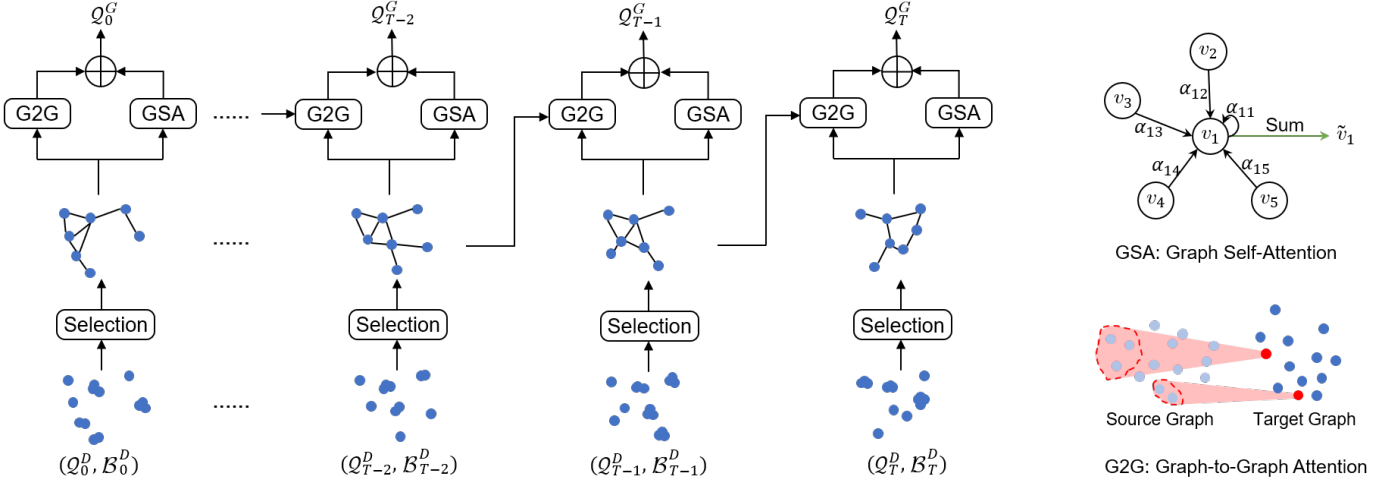


Fig. 4: Flowchart of the spatial-temporal graph attention network. First, we perform *graph node selection* to suppress redundant query boxes and select representative ones from the candidate boxes as nodes in the graph. Then we use the graph self-attention to model the social interaction between objects. To effectively capture temporal dependencies across different frames, we incorporate the graph-to-graph attention network that enables message passing from source graph (preceding frame) to target graph (current frame). Then the spatial and temporal features are added to obtain new encodings for refining the queries.

Algorithm 1: Graph Node Selection

- 1 **Input:** $\mathcal{B}_t^D = \{b_{t,i}^D\}_{i=1}^{N_q}$, $\mathcal{S}_t^D = \{s_{t,i}^D\}_{i=1}^{N_q}$,
 $Q_t^D = \{q_{t,i}^D\}_{i=1}^{N_q}$ are the output bounding boxes, confidence scores, and queries of decoder.
 - 2 **for** $i \leftarrow 1$ **to** N_q **do**
 - 3 $\mathcal{N}_{b_{t,i}^D} = \{j \mid \text{IoU}(b_{t,i}^D, b_{t,j}^D) > \theta\}$;
 - 4 $m = \underset{j}{\text{argmax}} \{s_{t,j}^D \mid j \in \mathcal{N}_{b_{t,i}^D}\}$;
 - 5 **if** $\mathcal{N}_{b_{t,i}^D}$ **is not empty then**
 - 6 **if** $s_{t,i}^D < s_{t,m}^D$ **then**
 - 7 $\tilde{s}_{t,i}^D \leftarrow s_{t,i}^D \times (1 - \text{IoU}(b_{t,i}^D, b_{t,m}^D))$;
 - 8 **end**
 - 9 **end**
 - 10 **end**
 - 11 Select top N_g bounding boxes based on confidence
 scores: $\hat{\mathcal{B}}_t^D \leftarrow \{b_{t,i}^D\}_{i=1}^{N_g}$, $\hat{Q}_t^D \leftarrow \{q_{t,i}^D\}_{i=1}^{N_g}$;
 - 12 **return** $\hat{\mathcal{B}}_t^D, \hat{Q}_t^D$.
-

, where we suppress the scores of boxes that have more confident boxes around them [55]. Finally, with the confidence scores of all boxes updated, we select bounding boxes with top N_g scores. The filtered bounding boxes $\hat{\mathcal{B}}_t^D = \{b_{t,i}^D\}_{i=1}^{N_g}$ and the corresponding query embedding $\hat{Q}_t^D = \{q_{t,i}^D\}_{i=1}^{N_g}$ are sent to the subsequent spatial self-attention module and temporal cross-attention module for further processing.

Discussion. Unlike the NMS-series methods that rely on confidence ranking and are challenging to parallelize, our proposed method is highly parallelizable. Since each candidate box is only influenced by its neighboring bounding boxes, we can create N_q threads to process them concur-

rently. This parallel processing significantly improves the efficiency of our algorithm. Furthermore, our approach differs from traditional NMS-series methods in terms of the objective. The NMS post-processing improves the accuracy and efficiency of detectors by selecting the single best box and eliminating other duplicate bounding boxes, while our method aims to suppress redundant boxes and select representative ones from the candidate boxes as nodes in the graph and excessive inhibition may result in loss of essential node information.

3.3.2 Spatial Self-Attention Module

Given the selected output of the decoder for each time, we construct a spatial graph where each node corresponds to a query embedding. We define the spatial graph as $G_t^s = \{V_t^s, E_t^s\}$, where V_t^s is the set of nodes and E_t^s is the set of edges. Each node $v_{t,i}^s \in V_t^s$ corresponds to output query embedding $q_{t,i}^D$ of decoder. For each pair of nodes $(v_{t,i}^s, v_{t,j}^s)$ in V_t^s , we calculate the distance between the centers of the corresponding query boxes $b_{t,i}^D$ and $b_{t,j}^D$. If the distance between the two bounding boxes is below the defined threshold d_s , we add an edge between them to E_t^s . The edge indicates a spatial relationship or proximity between the corresponding query embeddings.

We use the graph attention network to capture spatial dependencies among the query embeddings in the spatial graph [39]. For a node $v_{t,i}^s$, we calculate the similarity coefficient between its neighbors and itself:

$$e_{ij} = f([W_1^s v_{t,i}^s || W_1^s v_{t,j}^s]), \quad (3)$$

where W_1^s is a learnable weight matrix, $||$ denotes concatenation f is a single-layer feedforward neural network that maps the concatenated high-dimensional features to a real number, and $\mathcal{N}_{v_{t,i}^s}$ is the set of neighboring nodes of $v_{t,i}^s$ in

the spatial graph. Then we can further obtain the attention coefficients between each pair of nodes:

$$\alpha_{ij} = \frac{\exp(\text{LReLU}(e_{ij}))}{\sum_{k' \in \mathcal{N}_{v_{t,i}^s}} \exp(\text{LReLU}(e_{ik'}))}, \quad (4)$$

where $\text{LReLU}(\cdot)$ is a leaky rectified linear activation function. The attention coefficients are used to compute a weighted sum of the feature vectors of neighboring nodes. Finally, the output of the spatial transformer is the sum of the original query embeddings $v_{t,i}^s$ and the computed feature vectors:

$$\tilde{v}_{t,i}^s = v_{t,i}^s + \sigma \left(\sum_{j \in \mathcal{N}_{v_{t,i}^s}} \alpha_{ij} W_2^s v_{t,j}^s \right), \quad (5)$$

where W_2^s is a learnable weight matrix, σ is a non-linear function. Overall, the spatial self-attention modules model the interaction between the nodes, i.e., the query embedding in the same timestamp.

3.3.3 Temporal Cross-Attention Module

To capture temporal dependencies among the output of the decoder for multiple timestamps, we utilize the graph-to-graph attention mechanism. Specifically, we use a GAT to model the temporal relationship between the source graph G_{t-1}^u at $(t-1)$ -th frame and the target graph G_t^u at t -th frame. Let $V_t^u = \{v_{t,i}^u\}_{i=1}^{N_g}$ be the set of nodes in the target graph, where each node $v_{t,i}^u$ corresponds to the query embedding $q_{t,i}^D$. Similarly, we use $V_{t-1}^u = \{v_{t-1,i}^u\}_{i=1}^{N_g}$ to denote the set of nodes in the source graph.

The graph-to-graph cross-attention modules perform message passing from source graph to target graph. For the node $v_{t,i}^u$, we obtain its output by:

$$\tilde{v}_{t,i}^u = v_{t,i}^u + \sigma \left(\sum_{j \in \mathcal{N}_{v_{t,i}^u}} \beta_{ij} W_1^u v_{t-1,j}^u \right), \quad (6)$$

where W_1^u is the learnable transformation weight matrix for the source graph, $\mathcal{N}_{v_{t,i}^u}$ is the neighboring nodes of $v_{t,i}^u$ in the source graph. And β_{ij} is the attention coefficient between i -th node of the source graph and j -th node of the target graph computed as:

$$\beta_{ij} = \frac{\exp(\text{LReLU}(f([W_{tgt}^u v_{t,i}^u || W_{src}^u v_{t-1,j}^u])))}{\sum_{k' \in \mathcal{N}_{v_{t,i}^u}} \exp(\text{LReLU}(f([W_{tgt}^u v_{t,i}^u || W_{src}^u v_{t-1,k'}^u])))}, \quad (7)$$

where W_{src}^u and W_{tgt}^u are the learnable transformation weight matrices for source and target graphs respectively.

Finally, we obtain the graph embedding by taking the sum of the output of the spatial self-attention module and temporal cross-attention module. This informative graph embedding is further passed to another prediction head, which we call the graph head, to achieve refined bounding boxes. In such wise, we are able to capture both spatial and temporal dependencies among the output of the decoder for multi frames, which helps to improve the accuracy of 3D object detection.

3.4 Temporal Query Recollection

Motivation. Current models like DETR [22] generate region proposals in the encoder, and the decoder progressively refines the bounding box predictions based on these queries initialized with the proposals. However, if the initial queries inferred from the encoder miss some corner cases, it is challenging to obtain accurate results for these cases through layer-by-layer refinement in the decoder. Although we enhance the BEV features learned by the encoder with a ConvGRU block, feature-level enhancement alone is not sufficient. To address this limitation, we propose a training strategy called temporal query recollection to enhance the initial queries of the decoder. Specifically, we incorporate the final predictions from the last frame as an additional query input for the decoder in the current frame. The reason behind employing this strategy is that challenging cases that were missed by the encoder at the current frame might be comparatively easier to detect in the preceding frame.

Let $\mathcal{B}_{t-1}^G = \{b_{t-1,i}^G\}_{i=1}^{N_g}$ and $\mathcal{S}_{t-1}^G = \{s_{t-1,i}^G\}_{i=1}^{N_g}$ denote the prediction boxes and scores from the graph head at last timestamp $t-1$. When initializing the queries input for decoder, we select top N_{res} scored boxes $\hat{\mathcal{B}}_{t-1}^G$ as the supplementary of prediction of encoder $\mathcal{B}_t^E = \{b_{t,i}^E\}_{i=1}^{N_p}$. The total number of initial query embeddings N_q for the decoder is $N_q = N_p + N_{\text{res}}$. The initial query embeddings \mathcal{Q}_t^0 for the decoder are derived as follows:

$$\mathcal{Q}_t^0 = \{q_{t,i}^0 = \text{PE}(b_{t,i}^0, s_{t,i}^0), i = 1, \dots, N_q\}, \quad (8)$$

where each initial query embedding $q_{t,i}^0$ is encoded from the bounding box $b_{t,i}^0$ and confidence $s_{t,i}^0$ through the position encoding (PE).

Consequently, this initialization strategy improves the recall rate of initial queries with respect to the ground-truth boxes and provides a strong starting point for refining the bounding box predictions in the current frame. Additionally, initializing the queries with extra predicted boxes from the previous frame promotes temporal consistency in graph-based learning. The TQR strategy helps handle challenging scenarios such as object occlusions, sudden disappearances, and other common difficulties encountered in 3D object detection.

3.5 IoU Regularization Term

The current DETR-like detectors employ a one-to-one Hungarian Matching method, where only the query with the highest IoU is matched to each ground truth box. Other queries that are close to the ground truth box but have smaller overlaps are considered negative samples. Thus, it is necessary to take the surrounding similar queries into consideration when determining if the query is the best match and whether suppression is required. However, the current detection loss supervision for each query does not take into account the surrounding queries. It poses a challenge for the network to distinguish between the matched query and other highly similar queries that are not the best match. Similar queries are insufficiently suppressed and turn into redundant prediction boxes. Furthermore, the presence of duplicate query boxes without Non-Maximum Suppression (NMS) can degrade detection accuracy.

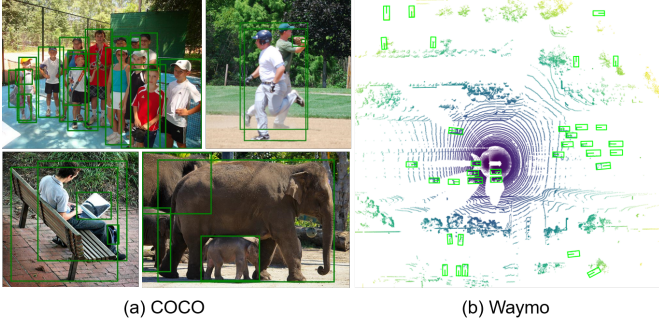


Fig. 5: Samples of the COCO dataset (left) and the Waymo dataset (right). The green boxes denote the ground truth bounding boxes. Unlike 2D detection, the bounding boxes in the Bird’s Eye View generally do not overlap in the 3D object detection task.

To address these issues, we propose the inclusion of an IoU regularization term to encourage diversity among the duplicate queries and discriminate similar object queries in local regions. This regularization term penalizes query boxes that are in close proximity to each other. By doing so, it encourages the unmatched queries to differentiate their predicted bounding boxes from the matched query during the refinement in decoder, even if they are highly similar. It is also worth noting that in 3D object detection tasks, unlike 2D detection, the bounding boxes in the Bird’s Eye View generally do not overlap (See Fig. 5). Therefore, the IoU regularization term does not affect the relationship between the matched queries as they do not overlap.

Specifically, we consider a specific FFN prediction head in our model that outputs a set of query boxes denoted as $\mathcal{B} = \{b_i\}_{i=1}^{N'}$. To promote diversity among the query boxes, we introduce a regularization loss term, denoted as \mathcal{R}_b , which is added to the overall loss function during model optimization. This term is computed by summing the IoU between each pair of bounding boxes, weighted by their corresponding confidence scores:

$$\mathcal{R}_b = \sum_{i=1}^{N'} \sum_{j=1, j \neq i}^{N'} s_i \times \text{IoU}(b_i, b_j), \quad (9)$$

where s_i is the corresponding confidence score of bounding box b_i . By incorporating this penalization, the model is encouraged to generate predictions with lower degrees of overlap, leading to increased diversity among the query boxes and improved distinguishability. The introduction of a confidence score aims to place more emphasis on bounding boxes that are close to the ground truth object with a high confidence score but are not the best match. These boxes are pushed further away from the best match, while boxes with lower confidence scores are considered less important and assigned lower weights.

3.6 Loss Function and Inference

Loss function. During training, we leverage the Hungarian algorithm to assign ground truths to the object queries in all FFN prediction heads in the encoder, decoder, and graph

head. Following [15], [54], we define the loss of each FFN prediction head as:

$$L = \lambda_{cls} L_{cls} + \lambda_h L_{Huber} + \lambda_{giou} L_{GIoU} + \lambda_r \mathcal{R}_b, \quad (10)$$

where we adopt the focal loss L_{cls} for classification, the Huber loss L_{Huber} and 3D GIoU loss L_{GIoU} are utilized for box regression, $\lambda_{cls}, \lambda_h, \lambda_{giou}, \lambda_r$ are hyper-parameters to balance the penalty terms.

Inference. For online multi-frame 3D object detection, we do not repeat all steps for the previous frames when we perform detection at current frame. Instead, we preserve useful variables during the detection of the last frame $t-1$. Specifically, when conducting detection at current time t , the hidden state H_{t-1} is used in ConvGRU modules to perform feature-level temporal enhancement, and the query embeddings inferred by the decoder in last frame $t-1$ are preserved to serve as nodes V_{t-1}^u in the source graph G_{t-1}^u to perform spatial-temporal message passing to target graph G_t^u . Therefore, the inference speed is not much slower than the single-frame detector.

4 EXPERIMENTS

In this section, we describe the datasets and evaluation metrics in Sec. 4.1, and introduce the implementation details in Sec. 4.2. Then we compare our method with previous state-of-the-art methods in Sec. 4.3. Afterward, thorough ablation studies are conducted to investigate the effectiveness of essential components of our framework in Sec. 4.4. Finally, we also provide the run-time efficiency analysis for online 3D object detection scenarios in Sec 4.6.

4.1 Dataset and Evaluation Metric

The Waymo Open Dataset [4] is a comprehensive and diverse dataset specifically designed for 3D object detection in autonomous driving scenarios. It consists of a large collection of 798 sequences for training, 202 sequences for validation, and 150 sequences for testing, resulting in a total of 198,438 LiDAR frames. Each sequence provides a rich set of data, including LiDAR point clouds, multi-view camera images, and object annotations spanning a full 360-degree field of view. Each sequence contains approximately 200 frames spanning 20 seconds. The Waymo dataset employs a 64-beam LiDAR with a capture frequency of 10Hz, resulting in around 180,000 points per frame. To facilitate the evaluation of 3D object detectors, the objects in the Waymo Open Dataset are categorized into two difficulty levels: LEVEL_L1, which represents objects with more than five observed LiDAR points, and LEVEL_L2, which includes objects with 1-5 points. The performance of 3D object detectors is commonly assessed using the mean Average Precision (mAP) and mean Average Precision weighted by heading accuracy (mAPH) metrics. For our experiments, we assess the detection results of objects in both LEVEL_L1 and LEVEL_L2 difficulty levels. We leverage the whole training set for supervision, and the evaluation is performed on the complete validation set, consisting of around 40,000 frames, using the official evaluation tool provided by Waymo. By leveraging the richness and diversity of the Waymo

Open Dataset, we aim to evaluate the performance of our approach for 3D object detection in autonomous driving scenarios, demonstrating its effectiveness in handling the challenges posed by real-world environments.

4.2 Implementation Details

Network architectures. In this part, we mainly elaborate the architectural details of the proposed model. First, we use average pooling to obtain the voxel-wise feature map by encoding the point cloud in each voxel. Then, our approach utilizes a ResNet18 [62] 3D backbone, which replaces the 2D convolution modules with 3D counterparts. We utilize the submanifold sparse convolution layers in all residual blocks except for the down-sampling layers, to reduce computational costs. To enhance the bird’s eye view features, we employ an FPN structure [63]. Then the 8x down-sampled BEV feature maps are then passed to a 3-layer encoder, where we incorporate BoxAttention [52], a variant of Deformable Attention [22], for self-attention operations. In the ConvGRU module after the encoder, we use a learnable kernel with a size of 3x3 for all convolution layers. The output of the ConvGRU module maintains the same channel configuration as the input BEV features. Leveraging the enhanced BEV features from the ConvGRU, we employ a class-agnostic FFN head to generate object proposals [54]. In the decoder, we perform standard multi-head attention for self-attention and BoxAttention for cross-attention between queries and BEV feature maps. We set the hidden size for encoder and decoder to 256, and the number of attention heads to 8. During training, we adopt a strategy called temporal query recollection, as described in Sec. 3.4. This strategy involves selecting the top 300 highest-scoring final predicted results from the previous frame to initialize the object queries of decoder. These queries act as a supplement to the top 1000 scored proposals generated by encoder in the current frame. In the graph node selection, we set the number of selected bounding boxes N_g to 800 and IoU threshold θ to 0.5. When it comes to the spatial-temporal graph attention network, we adopt the distance threshold $d_s = 2m$ and $d_u = 2m$ when determining the neighborhood of the node in the spatial self-attention module and temporal graph-to-graph attention network, respectively. In each FFN prediction head, we apply two separate 3-layer MLPs as prediction branches for classification and regression, respectively. For the loss function, the values for λ_{cls} , λ_h , λ_{giou} is set to 1, 4, 2, respectively. And the value of λ_r is set to 1 for the prediction head of decoder and the graph head, 0 for the proposal head in encoder.

Training details. For the input of model, we consider the points whose coordinates locate within [-75.2m, 75.2m], [-75.2m, 75.2m], and [-2m, 4m] along the x , y , and z axis respectively. And the point clouds are voxelized with (0.1m, 0.1m, 0.15m) grid size. The max number of non-empty voxels is set to 15000 during training and inference. We adopted the Adam optimizer with $\beta_1 = 0.9$ and $\beta_2 = 0.99$. We initialized the learning rate as 0.003 and updated it with the one-cycle scheduler [64] and weight decay of 0.01. And we trained the model for a total of 12 epochs in an end-to-end manner. The implementation is based on the PyTorch

framework. We set the score threshold to 0.1 to filter low-quality predictions during inference.

4.3 Comparison with State-of-the-Art Methods

In our study, we conduct a comparison between STEM, our proposed method, and the current state-of-the-art methods for 3D object detection. It can be observed in Table 1 that approaches employing multiple frames generally outperformed those using a single frame as input. When comparing our method to our previous state-of-the-art single-frame method, PV-RCNN++, our proposed STEM achieved a significant improvement in the overall 3D mAPH by utilizing an 8-frame point cloud sequence as input. Specifically, we observed remarkable enhancements in the detection performance for vehicles, pedestrians, and cyclists, with respective improvements of 1.5% mAPH, 6.1% mAPH, and 6.9% mAPH on LEVEL_2. Comparing our approach to previous single-frame detectors, the progress achieved by STEM validates its capability to successfully leverage the spatiotemporal dependencies, aiding in the accurate estimation of objects that are challenging to detect in the setting of single-frame input. Moreover, our method demonstrated superiority even when compared to the previous best-performing multi-frame approach, CenterFormer [48]. By employing our method, we were able to achieve a notable improvement of 4.8% mAPH on LEVEL_2 for the cyclist category. Additionally, our method exhibited improved performance when using shorter input sequences. Notably, even with a 4-frame input, our approach outperformed both the current single-frame and multi-frame methods. Specifically, we observed superior performance compared to PV-RCNN++ and CenterFormer, with improvements of 3.1% and 1.7% mAPH on LEVEL_1. Furthermore, it is important to highlight that our method is an end-to-end solution, distinguishing it from certain high-accuracy but two-phase methods [10], [11]. Overall, the results in Table 1 highlight the efficacy of STEM in effectively integrating temporal information from point cloud sequences, leading to enhanced detection accuracy compared to both single-frame and multi-frame methods.

4.4 Ablation Studies

We conducted ablative analyses to verify the effectiveness and characteristics of our processing pipeline. In the absence of special instructions, we use 4-frame point cloud input unless otherwise specified in this part. We report the APH on LEVEL_2 for vehicle, pedestrian, and cyclist categories and the mAPH metric for comparison.

Effect of key components. In Table 2, we investigate the effect of each added component in our method on the setting of 4-frame sequence input.

- As can be seen from the 1st row and 2nd row in Table 2, after changing the processing of multi-frame point cloud input from direct concatenation to operating it as a sequence, the results suggest an improvement and reaches 70.1% LEVEL_2 mAPH. This indicates that compared with the simple concatenation, the feature-level enhancement by the ConGRU block benefits the network in capturing the spatial-temporal dependencies. This also motivates us to

TABLE 1: Comparison with state-of-the-art methods on the validation set of Waymo Open Dataset (train with 100% training data). The best and second-best results are highlighted in **bold** and underlined, respectively.

Methods	Present at	Frames	mAP/mAPH		Cyclist 3D AP/APH		Pedestrian 3D AP/APH		Vehicle 3D AP/APH	
			L1	L2	L1	L2	L1	L2	L1	L2
SECOND [1]	Sensors'18	1	67.2/63.1	61.0/57.2	60.6/59.3	58.3/57.0	68.7/58.2	60.7/51.3	72.3/71.7	63.9/63.3
PointPillars [2]	CVPR'19	1	69.0/63.5	62.8/57.8	64.4/62.3	61.9/59.9	70.6/56.7	62.8/50.3	72.1/71.5	63.6/63.1
PV-RCNN [3]	CVPR'20	1	76.2/73.6	69.6/67.2	71.5/70.3	69.0/67.8	79.2/73.0	70.4/64.7	78.0/77.5	69.4/69.0
Part-A2-Net [56]	TPAMI'20	1	73.6/70.3	66.9/63.8	68.6/67.4	66.1/64.9	75.2/66.9	66.2/58.6	77.1/76.5	68.5/68.0
LiDAR-RCNN [57]	CVPR'21	1	71.9/63.9	65.8/61.3	68.6/66.9	66.1/64.4	71.2/58.7	63.1/51.7	76.0/75.5	68.3/67.9
CenterPoint [6]	CVPR'21	1	-/-	-/-	-/-	-/-	79.0/72.9	71.0/65.3	76.7/76.2	68.8/68.3
CenterPoint-TS [6]	CVPR'21	1	74.4/71.7	68.2/65.8	72.3/71.1	69.7/68.5	76.6/70.5	68.8/63.2	74.2/73.6	66.2/65.7
RangeDet [32]	ICCV'21	1	71.5/69.5	65.0/63.2	65.7/64.4	63.3/62.1	75.9/71.9	67.6/63.9	72.9/72.3	64.0/63.6
SST [33]	CVPR'22	1	74.5/71.0	67.8/64.6	70.7/69.6	68.0/66.9	78.7/69.6	70.0/61.7	74.2/73.8	65.5/65.1
VoxSet [58]	CVPR'22	1	75.4/72.2	69.1/66.2	71.6/70.3	69.0/67.7	80.0/72.4	72.5/65.4	74.5/74.0	66.0/65.6
SST-TS [33]	CVPR'22	1	-/-	-/-	-/-	-/-	81.4/74.0	72.8/65.9	76.2/75.8	68.0/67.6
AFDetV2 [59]	AAAI'22	1	77.2/74.8	71.0/68.8	73.7/72.7	71.0/70.1	80.2/74.6	72.2/67.0	77.6/77.1	69.7/69.2
SWFormer [50]	ECCV'22	1	-/-	-/-	-/-	-/-	80.9/72.7	72.5/64.9	77.8/77.3	69.2/68.8
PillarNet-34 [60]	ECCV'22	1	77.3/74.6	71.0/68.5	72.3/71.2	69.7/68.7	80.6/74.0	72.3/66.2	79.1/78.6	70.9/70.5
CenterFormer [48]	ECCV'22	1	75.3/72.9	71.1/68.9	73.3/71.3	69.8/68.8	78.6/73.0	73.6/68.3	75.0/74.4	69.9/69.4
PV-RCNN++ [61]	IJCV'22	1	78.1/75.9	71.7/69.5	72.7/72.7	71.2/70.2	81.3/76.3	73.2/68.0	79.3/78.8	70.6/70.2
Voxel-DETR [54]	CVPR'23	1	74.9/72.0	68.8/66.1	71.7/70.5	69.0/67.9	77.6/70.5	69.7/63.1	75.4/74.9	67.8/67.2
3D-MAN [7]	CVPR'21	16	-/-	-/-	-/-	-/-	71.7/67.7	62.6/59.0	74.5/74.0	67.6/67.1
CenterPoint [6]	CVPR'21	4	76.4/74.9	70.8/69.4	73.7/73.0	71.6/70.9	78.9/75.6	71.7/68.6	76.7/76.2	69.1/68.6
PillarNet-34 [60]	ECCV'22	2	77.6/76.2	71.8/70.4	70.5/69.7	68.4/67.6	82.5/79.3	75.0/72.0	80.0/79.5	72.0/71.5
CenterFormer [48]	ECCV'22	2	78.3/76.7	74.3/72.8	76.6/75.7	74.2/73.3	81.4/78.0	76.7/73.4	77.0/76.5	72.1/71.6
CenterFormer [48]	ECCV'22	4	78.5/77.0	74.7/73.2	75.6/74.8	73.4/72.6	81.7/78.6	77.2/74.2	78.1/77.6	73.4/72.9
CenterFormer [48]	ECCV'22	8	78.7/77.3	75.1/73.7	75.2/74.4	73.2/72.3	82.1/79.3	77.8/75.0	78.8/78.3	74.3/73.8
Ours (STEMD)	-	4	<u>80.7/79.0</u>	<u>75.3/73.7</u>	80.0/78.9	77.8/76.8	<u>83.5/80.1</u>	76.9/73.6	78.5/78.0	71.3/70.8
Ours (STEMD)	-	8	81.1/79.5	75.9/74.3	80.3/79.2	78.1/77.1	83.7/80.3	<u>77.4/74.1</u>	<u>79.4/78.8</u>	72.2/71.7

TABLE 2: Contribution of each component in the proposed method. The results of mAPH on LEVEL_2 are reported. "S.I." denotes the sequential point cloud input. "S.T." denotes spatial-temporal graph attention network. "TQR" means the temporal query recollection strategy. "IoU Reg" is the IoU regularization term in the loss function.

S.I.	S.T.	TQR	IoU Reg.	Veh.	Ped.	Cyc.	Mean
				68.33	67.36	71.16	69.62
✓				68.41	69.82	72.06	70.10
✓	✓			68.71	72.10	75.64	72.15
✓	✓	✓		69.30	73.30	76.01	72.87
✓	✓	✓	✓	70.83	73.62	76.80	73.75

take full advantage of the point cloud sequence and capture the spatial-temporal dependencies at not only the feature level but also the query level.

- When the spatial-temporal graph attention network is applied, we can further improve the result of vehicle, pedestrian, and cyclist by 0.3%, 2.28%, and 3.58% LEVEL_2 mAPH respectively. The improvement on the pedestrian and cyclist categories is more significant. We attribute this improvement to the interaction patterns exploited by the graph attention network, which effectively captures valuable information regarding the social behaviors exhibited by objects. This mechanism proves influential in complex scenarios, displaying a pronounced impact on categories such as pedestrians and cyclists.
- As reported in the fourth row of Table 2, the strategy of temporal query recollection yields an improvement of 0.72% mAPH, indicating the effectiveness of supplementing the queries initialized with boxes predicted by the encoder of current frame with the

TABLE 3: The results comparison of our STEMMD with the baseline [54] using point concatenation strategy under different frame length settings. We report the results of APH on LEVEL_2 for three categories.

Frames	Method	Veh.	Ped.	Cyc.	Mean
2	Concat.	68.12	67.74	71.38	69.08
	Ours	69.03	69.82	72.45	70.43
	<i>Improvement</i>	+0.91	+2.08	+1.07	+1.35
4	Concat.	68.33	69.36	71.16	69.62
	Ours	70.83	73.62	76.80	73.75
	<i>Improvement</i>	+2.50	+4.26	+5.64	+4.13
8	Concat.	69.25	69.76	70.02	69.68
	Ours	71.74	74.09	77.07	74.30
	<i>Improvement</i>	+2.49	+4.33	+7.05	+4.62
16	Concat.	69.12	69.82	70.02	69.65
	Ours	72.10	74.37	77.22	74.56
	<i>Improvement</i>	+2.98	+4.55	+7.20	+4.91

final prediction in last frame.

- As shown in the last row of Table 2, by introducing the IoU regularization term in the loss function of FFN prediction head, the performance will increase by 0.88% LEVEL_2 mAPH.

Effect of our multi-frame design. As shown in Table 3, we show the improvement of our multi-frame design compared to the baseline [54] using simple point cloud concatenation strategy under different settings of frame length. We can observe that the baseline does not perform well in modeling the long-term relations among frames as the performance slightly deteriorates when the number of concatenated frames increases from 8 to 16. In contrast, our proposed STEMMD achieves consistent improvements when the frame length increases. Specifically, our proposed STEMMD achieves 1.35%, 4.13%, 4.62%, and 4.91% higher mAPH than the

TABLE 4: Comparison of STGA-Net and conventional multi-head self-attention. We report the results of APH on LEVEL_2 for three categories.

Setting	Veh.	Ped.	Cyc.	Mean
STGA-Net	70.83	73.62	76.80	73.75
Self-Attention	70.60	71.24	73.71	71.85
Diff	-0.23	-2.38	-3.09	-1.90

TABLE 5: Effect of the number of nodes N_g adopted in STGA-Net. We report the recall rate of nodes in the graph with respect to the ground-truth bounding boxes at IoU thresholds of 0.7 and 0.5. We also report the results of APH on LEVEL_2 for three categories.

N_g	Recall@0.7	Recall@0.5	Veh.	Ped.	Cyc.	Mean
1300	88.11	97.05	70.47	72.23	75.22	72.64
1000	87.68	97.04	70.86	73.35	76.73	73.65
800	87.10	96.95	70.83	73.62	76.80	73.75
500	85.75	96.56	70.03	73.65	76.75	73.47
300	84.64	96.10	69.87	73.69	75.39	72.98

multi-frame baseline using point concatenation with 2, 4, 8, and 16 frames. The results demonstrate the effectiveness of our method in leveraging long-term temporal dependencies across multi frames.

Effect of the spatial-temporal graph attention network.

To showcase the effectiveness of the spatial-temporal graph attention network, we conducted additional experiments where we replaced it with conventional multi-head self-attention modules [44]. The results, as presented in Table 4, demonstrate that the normal multi-head self-attention mechanism performs 0.23%, 2.38%, and 3.09% worse in LEVEL_2 mAPH for cars, pedestrians, and bicycles categories, respectively, compared to the proposed spatial-temporal graph attention network. This indicates that the complex spatial-temporal dependencies between objects are more effectively modeled by the graph structure, which dynamically and contextually captures the relationships, as opposed to the self-attention mechanism that is densely applied across all queries.

Effect of the IoU regularization term. As shown in Fig. 6, we conducted a qualitative comparison between the results of the full model of STEMMD (shown on the right side) and the baseline setting without the IoU regularization term (left side). Upon analysis, we observed that the predictions of the baseline model exhibited highly-overlapped bounding boxes, which are highlighted with red circles. In contrast, the full model produced a single matched box for each object. This observation suggests that the introduction of the regularization term in the full model helps to push other close but unmatched queries away from the best-matched queries during the refinement in the decoder, and consequently leads to less-overlapped box predictions.

Hyper-parameters of graph node selection. In our approach, we incorporate graph node selection to address the issue of overlapping bounding boxes and associated queries generated by the decoder. This process results in a more streamlined graph structure for downstream graph-

TABLE 6: Effect of the number of queries in decoder initialized by the box predictions in last frame, i.e., N_{res} . We report the recall rate of all queries input for the decoder with respect to the ground-truth bounding boxes at IoU thresholds of 0.7 and 0.5. We also report the results of APH on LEVEL_2 for three categories.

N_{res}	Recall@0.7	Recall@0.5	Veh.	Ped.	Cyc.	Mean
0	68.89	88.80	70.28	72.66	76.41	73.12
100	69.06	89.00	70.51	72.95	76.49	73.32
200	69.45	89.22	70.74	73.50	76.55	73.60
300	69.75	89.31	70.83	73.62	76.80	73.75
500	69.76	89.36	70.79	73.64	76.82	73.75
800	69.81	89.39	70.71	73.66	76.85	73.74

based learning. However, it is crucial to determine the appropriate number of filtered bounding boxes, denoted as N_g , as an excessively large value can introduce redundant bounding boxes that impede the effectiveness of graph-based learning. Conversely, setting N_g too small may result in a lower recall rate of queries with respect to the ground-truth boxes. By analyzing Table 5, we observe a significant decrease in the recall rate at the 0.5 IoU threshold, dropping from 96.95% to 96.56% when N_g is reduced from 800 to 500. Thus, we find that setting N_g to 800 strikes a balance between recall and redundancy within the graph, thereby leading to the best detection accuracy of 73.75% mAPH.

Hyper-parameters of temporal query recollection. As shown in Table 6, with extra N_{res} queries initialized with boxes predicted at last frame, both the recall of all queries input for decoder with respect to the ground-truth bounding boxes and the overall mAPH improves. Specifically, the recall increases from 68.89% to 69.75% and from 88.80% to 89.31% at 0.7 and 0.5 IoU thresholds, respectively. But when we further increase the N_{res} from 300 to 500 or 800, neither the recall nor the detection accuracy improves significantly. Therefore, we can infer the collected queries in last frame could effectively supplement the output of encoder in current timestamp as extra input queries of decoder. And the value of N_{res} is important because too many recollected queries are helpless and could lead to unnecessary computation load.

Conditional analysis. To better figure out where our approach brings improvements, we compared STEMMD with the baseline that simply concatenates the multi-frame point clouds on objects of different speeds in Fig. 7. We can observe that the baseline model, based on the concatenation of 4 frames, achieves marginal improvement compared with the single-frame detector, and the performance on the slow category even deteriorates. Meanwhile, our proposed STEMMD achieves consistent improvements throughout all categories. Especially, our method outperforms the single-frame baseline by 5.3% and 5.9% APH improvement on medium and fast objects, the boost is more significant than that on stationary and slow categories. This observation demonstrates our proposed STEMMD effectively captures the temporal information about the motion and behavior of fast-moving objects across different frames.

Effect of the radius used to determine neighbors. Table 7

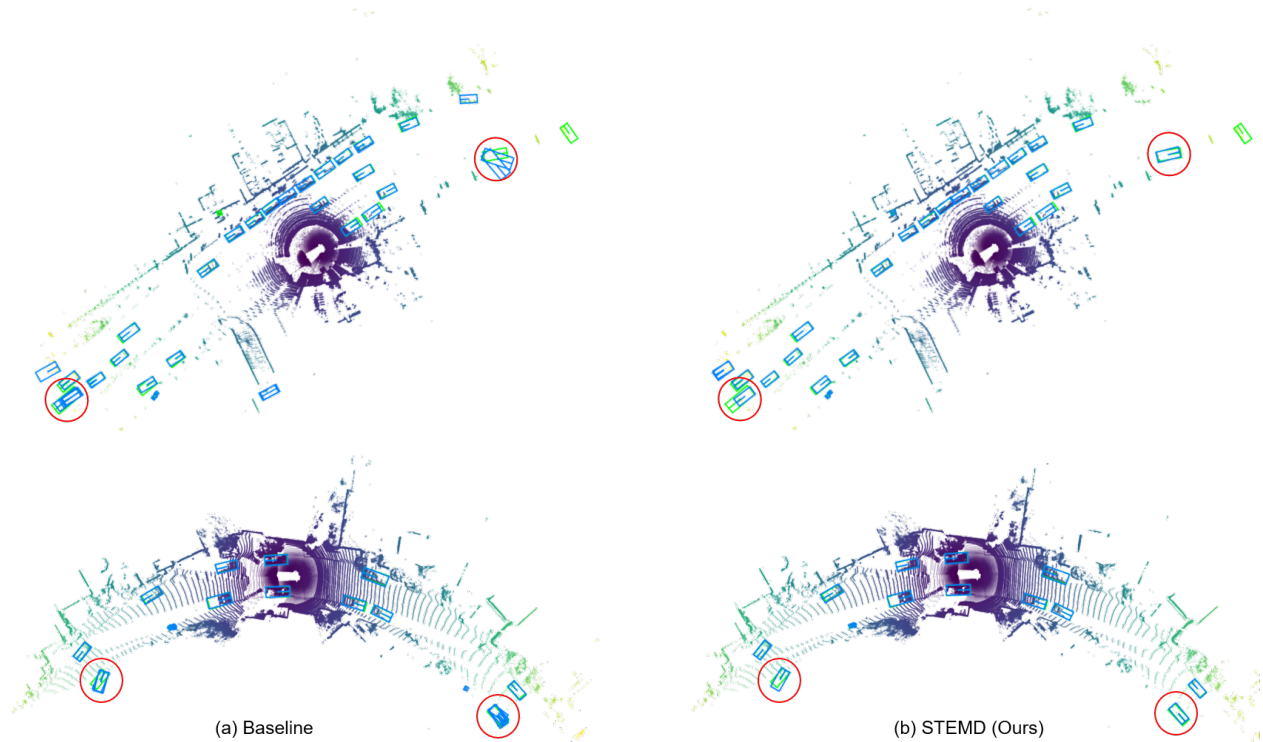


Fig. 6: Visual comparison of the full model of STEMMD (right) with the baseline setting w/o IoU regularization term. The green boxes represent the ground truth bounding boxes, while the blue boxes indicate the bounding box predictions with confidence larger than 0.1. The results of the baseline contain several overlapped boxes, while the full model generates sparser predictions (highlighted in the red circles).

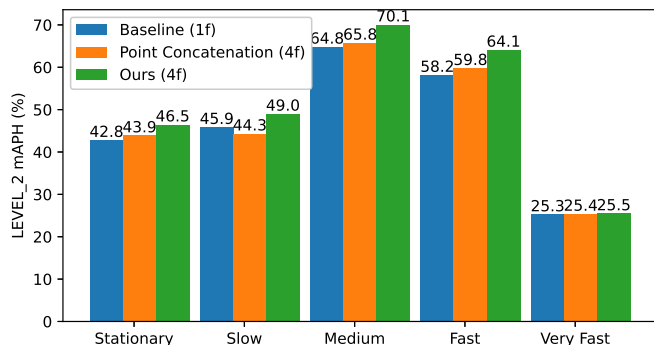


Fig. 7: The performance (mAPH) breakdown over different speeds. As defined by the official evaluation tools of Waymo dataset, objects can be classified based on their speed as follows: stationary (less than 0.2 m/s), slow (0.2 to 1 m/s), medium (1 to 3 m/s), fast (3 to 10 m/s), or very fast (greater than 10 m/s).

presents the results of an ablation study that investigates the effect of different radii for identifying neighbors of nodes in the spatial-temporal graph attention network. We can observe that the performance varies with different radii values. For example, for the vehicle class, the accuracy increases from 70.36% (radius 1) to 70.83% (radius 2) and then slightly decreases for radius 3 (70.47%) and radius 4

TABLE 7: The effects of different radii for identifying the neighbors of nodes in STGA-Net. The table shows the APH for three classes, as well as the mean performance across all classes (mAPH).

Radius	Veh.	Ped.	Cyc.	Mean
1	70.36	72.84	74.82	72.67
2	70.83	73.62	76.80	73.75
3	70.47	73.31	76.83	73.54
4	69.69	71.87	75.28	72.28

(69.69%). Similarly, for pedestrians and cyclists, the highest performance is achieved at radius 2, followed by a slight decrease for larger radii. Based on these findings, we can conclude that the choice of radius has an impact on the performance of the STGA-Net. It appears that a radius setting of 2 is more effective in learning spatial-temporal relations and yields the best overall results across all classes.

4.5 Visualization and Analysis

We present a qualitative analysis highlighting the advantages of our proposed method, STEMMD, for the multi-frame 3D object detection task. Specifically, we compare STEMMD with the baseline approach [54] using concatenated points as input, as shown in Fig. 8. In the first row of Fig. 8, we encounter a scene featuring a row of parked vehicles in the upper left area. While the baseline method falls short in detecting these distant and highly-occluded vehicles, our



Fig. 8: Illustration of a visual comparison between the results obtained by the multi-frame baseline [54] method utilizing point concatenation and our proposed STEM on the Waymo Open Dataset validation set. The ground-truth bounding boxes are shown in green, while the predicted bounding boxes are depicted in blue. To provide a comprehensive analysis, we employ red circles to highlight objects that were successfully detected by STEM but missed by the baseline approach. Additionally, we use orange circles to emphasize certain objects where the baseline method produces false-positive or redundant bounding boxes, while STEM accurately predicts correct and sparser bounding boxes. Best viewed in color and zoom in for more details.

STEMD model successfully localizes them with precision (highlighted by the red circles). Additionally, STEMD significantly reduces the number of false positives and redundant boxes (indicated by the orange circles). Similarly, in the second scene collected on a city street with densely parked vehicles surrounded by buildings, STEMD demonstrates its superiority in detecting distant and highly-occluded objects. This serves as a testament to the robustness of our method in challenging environments. Furthermore, in the third row of Fig. 8, STEMD accurately detects a vehicle on the right side, despite being highly occluded by other vehicles. This precision in estimation can be attributed to the learned relevant past location information and the coherence of object trajectories captured by your method. Overall, these examples effectively illustrate the advantages of your proposed STEMD method in precisely locating challenging objects, such as distant and highly-occluded ones, while also reducing the number of false-positive boxes. These improvements are achieved by leveraging spatial-temporal dependencies and learning from past location information.

4.6 Efficiency Analysis

Memory Efficiency. As mentioned in Sec. 3.6, our method only additionally employs a small set of features derived in last frame, which means that the additional memory required for storing these features is low. Besides, while some methods directly deal with concatenated multi-frame point clouds, the proposed method only takes the point cloud of the current frame as input. This reduces the number of points that need to be processed for detection, resulting in lower memory requirements during inference. Quantitatively, our method consumes 4170M of GPU memory during inference, which is only slightly higher than the single-frame method’s usage of 3470M when the batch size is set to 1. By emphasizing these specific measurements, we can confidently conclude that the STEMD method remains memory efficient.

Computation Efficiency. In the online multi-frame 3D object detection using STEMD, frames are processed sequentially in a streaming fashion. To avoid redundant computations, a small set of features computed in the last frame is reused. This results in a minor additional computational overhead, primarily from the STGA-Net and ConvGRU modules. Despite the additional computations, STEMD introduces only a small computational overhead. On a single NVIDIA A100 GPU, it achieves a latency of 88 ms, assuming that the features from preceding frames are already available in memory. Compared to the single-frame baseline latency of 70 ms, our method incurs a modest 25% increase in latency while significantly improving detection accuracy. It is worth noting that given the typical LiDAR scan frequency of 10 Hz, our network remains capable of operating in real-time scenarios within its 100 ms computation budget.

4.7 Further Discussions

While our experiments have demonstrated the significant benefits of leveraging spatial-temporal information for 3D object detection, it is important to acknowledge the limitations of our current approach. One key limitation is that

our method falls short in terms of performance compared to some state-of-the-art two-phase methods [10], [11]. It is worth highlighting that the DETR-like paradigm has already surpassed CNN-based detectors and achieved state-of-the-art performance in the 2D object detection task. However, in the context of 3D object detection, our proposed model, STEMD, should be considered as a baseline for future, more powerful DETR-like models. There is still tremendous potential to be explored, as our framework has not incorporated several advanced techniques that have shown promising results in 2D DETR-like models [18], [65], [66].

Another limitation of our method is the lack of obvious improvement in detecting objects that are moving at high speeds. We attribute this result to the fact that we did not explicitly consider the motion of fast-moving objects in our spatial-temporal modeling. Even though the time interval between each frame is only 100 ms, objects moving at high speeds can cover significant distances within this short time period. As a result, STGA-Net, our proposed model, fails to effectively capture the spatial-temporal dependencies between these fast-moving objects and their neighboring objects. In future research, it would be valuable to explore methods that can better handle the detection of fast-moving objects. Techniques such as motion estimation could be incorporated into the spatial-temporal modeling process to capture the dynamics of these objects more accurately. Additionally, investigating the use of higher frame rates or adaptive frame sampling strategies may help alleviate the issue of fast-moving objects being poorly represented in the temporal context.

In all, while our study has demonstrated the potential of spatial-temporal information for 3D object detection, there is still work to be done to improve the performance of our approach. By drawing inspiration from recent advancements in 2D DETR and addressing the challenges posed by fast-moving objects, future iterations of DETR-like models hold great promise for achieving even higher accuracy and robustness in multi-frame 3D object detection tasks.

5 CONCLUSION

In this paper, we have presented STEMD, a novel end-to-end multi-frame 3D object detection framework based on the DETR-like paradigm. Our approach effectively models inter-object spatial interaction and complex temporal dependencies by introducing the spatial-temporal graph attention network, representing queries as nodes in a graph. Additionally, we improve the detection process by incorporating the detection results from the previous frame to enhance the query input of the decoder. Furthermore, based on the characteristics of 3D inspection tasks, we further incorporate the IoU regularization term in the loss function to reduce redundancy in bounding box predictions. Through extensive experiments conducted on the Waymo dataset, our framework has demonstrated superior performance in 3D object detection tasks. The results validate the effectiveness of our proposed approach, showcasing the potential of modeling spatial-temporal relationships between objects in this domain.

TABLE A1: Main notations in this paper.

Notation	Definition
T	Length of point cloud sequence
t	The index of frame
I_t	The point cloud at t -th frame
X_t	Features output by CNN
H_t	Out of ConGRU at t -th frame
B_t^E	Proposal generated by encoder
N_p	Number of selected proposal
X_t^E	Features output by encoder
N_g	Number of object queries
Q_t^0	Initial Object queries at t -th frame
B_t^D	Boxes predicted by decoder
S_t^D	Confidence scores predicted by decoder
Q_t^D	Query embedding output by decoder
\hat{B}_t^D	Selected boxes for graph construction
\hat{Q}_t^D	Selected queries as nodes in the graph
N_g	Number of nodes in a graph
G_t^s	Spatial graph at t -th frame
V_t^s	The set of nodes in G_t^s
E_t^s	The set of edges in G_t^s
$v_{i,i}^s$	The i -th node in G_t^s
d_s	Distance threshold used to determine the presence of edges between nodes.
α_{ij}	Attention coefficient between i -th node and j -th node in spatial graph
β_{ij}	Attention coefficients between i -th node in target graph and j -th node in source graph
N_{res}	Number of queries input recollected from last frame
\mathcal{R}_b	IoU regularization term

APPENDIX A NOTATIONS

The notations used in this paper are summarized in Table A1.

REFERENCES

- [1] Y. Yan, Y. Mao, and B. Li, "Second: Sparsely embedded convolutional detection," *Sensors*, vol. 18, no. 10, p. 3337, 2018.
- [2] A. Lang, S. Vora, H. Caesar, L. Zhou, J. Yang, and O. Beijbom, "Pointpillars: Fast encoders for object detection from point clouds," in *Proceedings of the IEEE/CVF Conference on Computer Vision and Pattern Recognition*, 2019, pp. 12 689–12 697.
- [3] S. Shi, C. Guo, L. Jiang, Z. Wang, J. Shi, X. Wang, and H. Li, "Pv-rnn: Point-voxel feature set abstraction for 3d object detection," in *Proceedings of the IEEE/CVF Conference on Computer Vision and Pattern Recognition*, 2020, pp. 10 529–10 538.
- [4] P. Sun, H. Kretschmar, X. Dotiwalla, A. Chouard, V. Patnaik, P. Tsui, J. Guo, Y. Zhou, Y. Chai, B. Caine, V. Vasudevan, W. Han, J. Ngiam, H. Zhao, A. Timofeev, S. Ettinger, M. Krivokon, A. Gao, A. Joshi, Y. Zhang, J. Shlens, Z. Chen, and D. Anguelov, "Scalability in perception for autonomous driving: Waymo open dataset," in *Proceedings of the IEEE/CVF Conference on Computer Vision and Pattern Recognition*, 2020, pp. 2443–2451.
- [5] H. Caesar, V. Bankiti, A. H. Lang, S. Vora, V. E. Liong, Q. Xu, A. Krishnan, Y. Pan, G. Baldan, and O. Beijbom, "nuscenes: A multimodal dataset for autonomous driving," in *Proceedings of the IEEE/CVF Conference on Computer Vision and Pattern Recognition*, 2020, pp. 11 621–11 631.
- [6] T. Yin, X. Zhou, and P. Krahenbuhl, "Center-based 3d object detection and tracking," in *Proceedings of the IEEE/CVF Conference on Computer Vision and Pattern Recognition*, 2021, pp. 11 784–11 793.
- [7] Z. Yang, Y. Zhou, Z. Chen, and J. Ngiam, "3d-man: 3d multi-frame attention network for object detection," in *Proceedings of the IEEE/CVF Conference on Computer Vision and Pattern Recognition*, 2021, pp. 1863–1872.
- [8] J. Yin, J. Shen, C. Guan, D. Zhou, and R. Yang, "Lidar-based on-line 3d video object detection with graph-based message passing and spatiotemporal transformer attention," in *Proceedings of the IEEE/CVF Conference on Computer Vision and Pattern Recognition*, 2020, pp. 11 495–11 504.
- [9] R. Huang, W. Zhang, A. Kundu, C. Pantofaru, D. A. Ross, T. Funkhouser, and A. Fathi, "An lstm approach to temporal 3d object detection in lidar point clouds," in *European Conference on Computer Vision*, 2020, pp. 266–282.
- [10] X. Chen, S. Shi, B. Zhu, K. C. Cheung, H. Xu, and H. Li, "Mppnet: Multi-frame feature intertwining with proxy points for 3d temporal object detection," in *European Conference on Computer Vision*, 2022, pp. 680–697.
- [11] C. R. Qi, Y. Zhou, M. Najibi, P. Sun, K. Vo, B. Deng, and D. Anguelov, "Offboard 3d object detection from point cloud sequences," in *Proceedings of the IEEE/CVF Conference on Computer Vision and Pattern Recognition*, 2021, pp. 6134–6144.
- [12] J. Devlin, M.-W. Chang, K. Lee, and K. Toutanova, "Bert: Pre-training of deep bidirectional transformers for language understanding," in *Annual Conference of the North American Chapter of the Association for Computational Linguistics*, 2019, pp. 4171–4186.
- [13] J. Lu, D. Batra, D. Parikh, and S. Lee, "Vilbert: Pretraining task-agnostic visiolinguistic representations for vision-and-language tasks," *Advances in Neural Information Processing Systems*, vol. 32, 2019.
- [14] A. Prakash, K. Chitta, and A. Geiger, "Multi-modal fusion transformer for end-to-end autonomous driving," in *Proceedings of the IEEE/CVF Conference on Computer Vision and Pattern Recognition*, 2021, pp. 7077–7087.
- [15] N. Carion, F. Massa, G. Synnaeve, N. Usunier, A. Kirillov, and S. Zagoruyko, "End-to-end object detection with transformers," in *European Conference on Computer Vision*, 2020, pp. 213–229.
- [16] Z. Yang, Y. Sun, S. Liu, and J. Jia, "3dssd: Point-based 3d single stage object detector," in *Proceedings of the IEEE/CVF Conference on Computer Vision and Pattern Recognition*, 2020, pp. 11 040–11 048.
- [17] S. Ren, K. He, R. Girshick, and J. Sun, "Faster r-cnn: Towards real-time object detection with region proposal networks," *Advances in Neural Information Processing Systems*, vol. 28, pp. 91–99, 2015.
- [18] H. Zhang, F. Li, S. Liu, L. Zhang, H. Su, J. Zhu, L. Ni, and H.-Y. Shum, "DINO: DETR with improved denoising anchor boxes for end-to-end object detection," in *International Conference on Learning Representations*, 2023.
- [19] L. Li, M. Pagnucco, and Y. Song, "Graph-based spatial transformer with memory replay for multi-future pedestrian trajectory prediction," in *Proceedings of the IEEE/CVF Conference on Computer Vision and Pattern Recognition*, 2022, pp. 2231–2241.
- [20] C. Yu, X. Ma, J. Ren, H. Zhao, and S. Yi, "Spatio-temporal graph transformer networks for pedestrian trajectory prediction," in *European Conference on Computer Vision*, 2020, pp. 507–523.
- [21] Y. Wang, S. Zhao, R. Zhang, X. Cheng, and L. Yang, "Multi-vehicle collaborative learning for trajectory prediction with spatio-temporal tensor fusion," *IEEE Transactions on Intelligent Transportation Systems*, vol. 23, no. 1, pp. 236–248, 2020.
- [22] X. Zhu, W. Su, L. Lu, B. Li, X. Wang, and J. Dai, "Deformable detr: Deformable transformers for end-to-end object detection," in *International Conference on Learning Representations*, 2021.
- [23] Y. Zhou and O. Tuzel, "Voxelnet: End-to-end learning for point cloud based 3d object detection," in *Proceedings of the IEEE/CVF Conference on Computer Vision and Pattern Recognition*, 2018, pp. 4490–4499.
- [24] J. Deng, S. Shi, P. Li, W. Zhou, Y. Zhang, and H. Li, "Voxel r-cnn: Towards high performance voxel-based 3d object detection," in *Proceedings of the AAAI Conference on Artificial Intelligence*, 2021, pp. 1201–1209.
- [25] S. Shi, X. Wang, and H. Li, "Pointcnn: 3d object proposal generation and detection from point cloud," in *Proceedings of the IEEE/CVF Conference on Computer Vision and Pattern Recognition*, 2019, pp. 770–779.
- [26] C. R. Qi, L. Yi, H. Su, and L. J. Guibas, "Pointnet++: Deep hierarchical feature learning on point sets in a metric space," *Advances in Neural Information Processing Systems*, vol. 30, 2017.
- [27] Y. Zhang, Q. Hu, G. Xu, Y. Ma, J. Wan, and Y. Guo, "Not all points are equal: Learning highly efficient point-based detectors for 3d lidar point clouds," in *Proceedings of the IEEE/CVF Conference on Computer Vision and Pattern Recognition*, 2022, pp. 18 953–18 962.
- [28] C. Chen, Z. Chen, J. Zhang, and D. Tao, "Sasa: Semantics-augmented set abstraction for point-based 3d object detection,"

- in *Proceedings of the AAAI Conference on Artificial Intelligence*, vol. 1, 2022, pp. 221–229.
- [29] C. He, H. Zeng, J. Huang, X.-S. Hua, and L. Zhang, “Structure aware single-stage 3d object detection from point cloud,” in *Proceedings of the IEEE/CVF Conference on Computer Vision and Pattern Recognition*, 2020, pp. 11 873–11 882.
- [30] J. S. Hu, T. Kuai, and S. L. Waslander, “Point density-aware voxels for lidar 3d object detection,” in *Proceedings of the IEEE/CVF Conference on Computer Vision and Pattern Recognition*, 2022, pp. 8469–8478.
- [31] Z. Liang, Z. Zhang, M. Zhang, X. Zhao, and S. Pu, “RangeiouDET: Range image based real-time 3d object detector optimized by intersection over union,” in *Proceedings of the IEEE/CVF Conference on Computer Vision and Pattern Recognition*, 2021, pp. 7140–7149.
- [32] L. Fan, X. Xiong, F. Wang, N. Wang, and Z. Zhang, “Rangedet: In defense of range view for lidar-based 3d object detection,” in *Proceedings of the IEEE/CVF International Conference on Computer Vision*, 2021, pp. 2918–2927.
- [33] L. Fan, Z. Pang, T. Zhang, Y.-X. Wang, H. Zhao, F. Wang, N. Wang, and Z. Zhang, “Embracing single stride 3d object detector with sparse transformer,” in *Proceedings of the IEEE/CVF Conference on Computer Vision and Pattern Recognition*, 2022, pp. 8458–8468.
- [34] Z. Wu, S. Pan, F. Chen, G. Long, C. Zhang, and S. Y. Philip, “A comprehensive survey on graph neural networks,” *IEEE transactions on neural networks and learning systems*, vol. 32, no. 1, pp. 4–24, 2020.
- [35] T. N. Kipf and M. Welling, “Semi-supervised classification with graph convolutional networks,” in *International Conference on Learning Representations*, 2016, pp. 1–14.
- [36] J. Gilmer, S. S. Schoenholz, P. F. Riley, O. Vinyals, and G. E. Dahl, “Neural message passing for quantum chemistry,” in *International Conference on Machine Learning*. PMLR, 2017, pp. 1263–1272.
- [37] M. Niepert, M. Ahmed, and K. Kutzkov, “Learning convolutional neural networks for graphs,” in *International Conference on Machine Learning*. PMLR, 2016, pp. 2014–2023.
- [38] J. Bruna, W. Zaremba, A. Szlam, and Y. LeCun, “Spectral networks and locally connected networks on graphs,” in *International Conference on Learning Representations*, 2013, pp. 1–12.
- [39] P. Velickovic, G. Cucurull, A. Casanova, A. Romero, P. Lio, and Y. Bengio, “Graph attention networks,” in *International Conference on Learning Representations*, 2017, pp. 1–12.
- [40] W. Hamilton, Z. Ying, and J. Leskovec, “Inductive representation learning on large graphs,” *Advances in Neural Information Processing Systems*, vol. 30, 2017.
- [41] H. Xu, C. Jiang, X. Liang, and Z. Li, “Spatial-aware graph relation network for large-scale object detection,” in *Proceedings of the IEEE/CVF Conference on Computer Vision and Pattern Recognition*, 2019, pp. 9298–9307.
- [42] K. Cheng, Y. Zhang, X. He, W. Chen, J. Cheng, and H. Lu, “Skeleton-based action recognition with shift graph convolutional network,” in *Proceedings of the IEEE/CVF Conference on Computer Vision and Pattern Recognition*, 2020, pp. 183–192.
- [43] Y. Chen, Z. Zhang, C. Yuan, B. Li, Y. Deng, and W. Hu, “Channel-wise topology refinement graph convolution for skeleton-based action recognition,” in *Proceedings of the IEEE/CVF International Conference on Computer Vision*, 2021, pp. 13 359–13 368.
- [44] A. Vaswani, N. Shazeer, N. Parmar, J. Uszkoreit, L. Jones, A. N. Gomez, Ł. Kaiser, and I. Polosukhin, “Attention is all you need,” *Advances in Neural Information Processing Systems*, vol. 30, 2017.
- [45] A. Radford, J. Wu, R. Child, D. Luan, D. Amodei, I. Sutskever *et al.*, “Language models are unsupervised multitask learners,” *OpenAI blog*, vol. 1, no. 8, p. 9, 2019.
- [46] A. Dosovitskiy, L. Beyer, A. Kolesnikov, D. Weissenborn, X. Zhai, T. Unterthiner, M. Dehghani, M. Minderer, G. Heigold, S. Gelly *et al.*, “An image is worth 16x16 words: Transformers for image recognition at scale,” in *International Conference on Learning Representations*, 2021.
- [47] Z. Liu, Y. Lin, Y. Cao, H. Hu, Y. Wei, Z. Zhang, S. Lin, and B. Guo, “Swin transformer: Hierarchical vision transformer using shifted windows,” in *Proceedings of the IEEE/CVF International Conference on Computer Vision*, 2021, pp. 10012–10022.
- [48] Z. Zhou, X. Zhao, Y. Wang, P. Wang, and H. Foroosh, “Centerformer: Center-based transformer for 3d object detection,” in *European Conference on Computer Vision*, 2022, pp. 496–513.
- [49] Y. Zeng, D. Zhang, C. Wang, Z. Miao, T. Liu, X. Zhan, D. Hao, and C. Ma, “Lift: Learning 4d lidar image fusion transformer for 3d object detection,” in *Proceedings of the IEEE/CVF Conference on Computer Vision and Pattern Recognition*, 2022, pp. 17 172–17 181.
- [50] P. Sun, M. Tan, W. Wang, C. Liu, F. Xia, Z. Leng, and D. Anguelov, “Swformer: Sparse window transformer for 3d object detection in point clouds,” in *European Conference on Computer Vision*, 2022, pp. 426–442.
- [51] H. Sheng, S. Cai, Y. Liu, B. Deng, J. Huang, X.-S. Hua, and M.-J. Zhao, “Improving 3d object detection with channel-wise transformer,” in *Proceedings of the IEEE/CVF International Conference on Computer Vision*, 2021, pp. 4773–4782.
- [52] D.-K. Nguyen, J. Ju, O. Booi, M. R. Oswald, and C. G. Snoek, “Boxer: Box-attention for 2d and 3d transformers,” in *Proceedings of the IEEE/CVF Conference on Computer Vision and Pattern Recognition*, 2022, pp. 4773–4782.
- [53] N. Ballas, L. Yao, C. Pal, and A. Courville, “Delving deeper into convolutional networks for learning video representations,” in *Proceedings of the IEEE/CVF International Conference on Computer Vision*, 2015, pp. 1–9.
- [54] B. Zhu, Z. Wang, S. Shi, H. Xu, L. Hong, and H. Li, “Conquer: Query contrast voxel-detr for 3d object detection,” *arXiv preprint arXiv:2212.07289*, 2022.
- [55] N. Bodla, B. Singh, R. Chellappa, and L. S. Davis, “Soft-nms—improving object detection with one line of code,” in *Proceedings of the IEEE/CVF International Conference on Computer Vision*, 2017, pp. 5561–5569.
- [56] S. Shi, Z. Wang, J. Shi, X. Wang, and H. Li, “From points to parts: 3d object detection from point cloud with part-aware and part-aggregation network,” *IEEE Transactions on Pattern Analysis and Machine Intelligence*, vol. 43, no. 8, pp. 2647–2664, 2020.
- [57] Z. Li, F. Wang, and N. Wang, “Lidar r-cnn: An efficient and universal 3d object detector,” in *Proceedings of the IEEE/CVF Conference on Computer Vision and Pattern Recognition*, 2021, pp. 7546–7555.
- [58] C. He, R. Li, S. Li, and L. Zhang, “Voxel set transformer: A set-to-set approach to 3d object detection from point clouds,” in *Proceedings of the IEEE/CVF Conference on Computer Vision and Pattern Recognition*, 2022, pp. 8417–8427.
- [59] Y. Hu, Z. Ding, R. Ge, W. Shao, L. Huang, K. Li, and Q. Liu, “Afdetv2: Rethinking the necessity of the second stage for object detection from point clouds,” in *Proceedings of the AAAI Conference on Artificial Intelligence*, 2022, pp. 969–979.
- [60] G. Shi, R. Li, and C. Ma, “PillarNet: Real-time and high-performance pillar-based 3d object detection,” in *European Conference on Computer Vision*, 2022, pp. 35–52.
- [61] S. Shi, L. Jiang, J. Deng, Z. Wang, C. Guo, J. Shi, X. Wang, and H. Li, “Pv-rnn++: Point-voxel feature set abstraction with local vector representation for 3d object detection,” *International Journal of Computer Vision*, vol. 131, no. 2, pp. 531–551, 2023.
- [62] K. He, X. Zhang, S. Ren, and J. Sun, “Deep residual learning for image recognition,” in *Proceedings of the IEEE/CVF Conference on Computer Vision and Pattern Recognition*, 2016, pp. 770–778.
- [63] T.-Y. Lin, P. Dollár, R. Girshick, K. He, B. Hariharan, and S. Belongie, “Feature pyramid networks for object detection,” in *Proceedings of the IEEE/CVF Conference on Computer Vision and Pattern Recognition*, 2017, pp. 2117–2125.
- [64] L. N. Smith, “Cyclical learning rates for training neural networks,” in *Proceedings of the IEEE/CVF Winter Conference on Applications of Computer Vision*. IEEE, 2017, pp. 464–472.
- [65] F. Li, H. Zhang, S. Liu, J. Guo, L. M. Ni, and L. Zhang, “Dn-detr: Accelerate detr training by introducing query denoising,” in *Proceedings of the IEEE/CVF Conference on Computer Vision and Pattern Recognition*, 2022, pp. 13 619–13 627.
- [66] F. Chen, H. Zhang, K. Hu, Y.-K. Huang, C. Zhu, and M. Savvides, “Enhanced training of query-based object detection via selective query recollection,” in *Proceedings of the IEEE/CVF Conference on Computer Vision and Pattern Recognition*, 2023, pp. 23 756–23 765.